remote sensing

MDPI

Communication

Compact Matrix-Exponential-Based FDTD with Second-Order PML and Direct Z-Transform for Modeling Complex Subsurface Sensing and Imaging Problems

Naixing Feng [1], Yuxian Zhang [1,*], Guo Ping Wang [1], Qingsheng Zeng [2] and William T. Joines [3]

[1] Institute of Microscale Optoelectronics, Shenzhen University, Shenzhen 518060, China; fengnaixing@szu.edu.cn (N.F.); gpwang@szu.edu.cn (G.P.W.)
[2] College of Astronautics, Nanjing University of Aeronautics and Astronautics, Nanjing 210016, China; qingshengzeng@nuaa.edu.cn
[3] Department of Electrical and Computer Engineering, Duke University, Durham, NC 27708, USA; william.joines@duke.edu
* Correspondence: yxzhang@szu.edu.cn; Tel.: +86-159-5927-3751

Abstract: To simulate complex subsurface sensing and imaging problems with both propagating and evanescent waves by the finite-difference time-domain (FDTD) method, the highly-accurate second-order perfectly matched layer (SO-PML) formulations based on the direct Z-transform (DZT) and the matrix exponential (ME) techniques are compactly and efficiently proposed for modeling open-domain problems. During mathematical deductions, several manipulations, for example, convolution computations, formulation reorganizations, or variable substitutions, can be circumvented due to the fact that the ME-based method shows a compact first-order differential matrix form. Besides, any material attributes can be completely circumvented because of using electric and magnetic flux densities, consequently, the proposed DZT-SO-PML could be applied without needing any alteration. Moreover, the DZT-SO-PML method can not only preserve better absorption accuracies, but also attain palpable improvements in computational efficiencies, even if the distance between the DSP-SO-PML truncation and the target becomes closer for modeling 3D open-domain subsurface sensing and imaging problems. Finally, numerical examples have been carried out to illustrate and validate these proposed formulations.

Keywords: direct Z-transform method; finite-difference time-domain method; matrix exponential; subsurface sensing and imaging; second-order perfectly matched layer

Citation: Feng, N.; Zhang, Y.; Wang, G.P.; Zeng, Q.; Joines, W.T. Compact Matrix-Exponential-Based FDTD with Second-Order PML and Direct Z-Transform for Modeling Complex Subsurface Sensing and Imaging Problems. *Remote Sens.* **2021**, *13*, 94. https://doi.org/10.3390/rs13010094

Received: 24 November 2020
Accepted: 27 December 2020
Published: 30 December 2020

1. Introduction

In modern communications, the radio wave in the air can transmit information for radio, radar, navigation systems and other applications [1–4]. However, limitations [5] have been found in shorter-wavelength radio waves whose signals become weaker and weaker when propagating farther and farther, even never transmit through water, and easily are prevented by the rock layer. For example, the global position system (GPS) [5] signals cannot penetrate into water, soil or building walls, or even can never propagate into these objects, So, the submarine or underground activities, such as mineral surveys, cannot adopt GPS signals. Besides, GPS and other radio signals work quite poorly in indoor rooms, or outdoor skyscrapers in between.

To overcome problems depicted above, nonetheless, the very low frequency (VLF) radio with the longer wavelength can be considered as an impactful approach [6]. As is well known to all, VLF waves have advantages of long-distance propagation and strong-power penetration [7], which can propagate and span over hundreds of feet in water and earth, and thousands of miles in air. Nowadays, the VLF signals have been widely applied in the military and civil fields, such as long-distance communication and navigation, wireless heart rate detectors, disaster relief, and submarine communication and geophysics research.

In many applications, the VLF geophysics exploration research is so few mentioned in the open-domain finite-difference time-domain (FDTD) numerical simulation, as investigations on the absorption performance of the perfectly matched layer (PML) for three-dimensional (3D) VLF subsurface sensing and imaging problems are quite rare in the literatures.

As far as we know, the traditional explicit finite-difference time-domain method has hitherto attracted great popularity as a quite efficacious tool for solving the Maxwell's equations, which are the effective and pinpoint solution of electromagnetic wave interaction problems [8]. With the rapid development of FDTD, it can be used for dealing with numerous types of applications, like antennas, waveguides, propagation, scattering, microwave circuits, non-linear and other special materials, and many other applications [9]. Nevertheless, to model open-domain problems, the split-field perfectly matched layer scheme [10], as one of the most popular and accurate absorbing boundary conditions (ABCs), is developed to truncate the physical domain due to the fact that computers can never store an unlimited amount of field data.

Afterward, several unsplit-field-based PML methods have been gradually adopted to replace previous PMLs in that much memory and computational time can be saved [11–15]. As with split-field PMLs above, nevertheless, strong evanescent waves can be ineffectively absorbed by unsplit-field ones. To avoid this case, therefore, the complex-frequency-shifted PML (CFS-PML) [16] is firstly proposed to attenuate low-frequency evanescent waves and reduce late-time reflections, leading to attracting substantial attention so much so that a large number of the literatures appears to apply this kind of technique [17–21].

To further conquer limitations of the above PMLs with/without CFS scheme, several higher-order PMLs [22–27] are presented, which can simultaneously absorb both strong propagating and evanescent waves. Moreover, among these higher-order PMLs, the second-order PML (SO-PML) [28] has been validated and proved to be a better selection, which not only requires less CPU time and memory, but also maintains almost the same absorption accuracies as compared with higher-order PMLs ($n > 2$).

For engineering applications in electromagnetics, as far as we know, the maximum relative reflection error with below -40 dB can reach engineering requirements. Consequently, to reduce unnecessary consumption in memory and CPU time, the unsplit-field CFS-PML based on the direct Z-transform (DZT) is proposed to achieve this goal [29]. Very recently, a modified CFS-PML implementation [30] using the matrix exponential (ME) technique is presented, which has a higher accuracy than presented CFS-PMLs and maintains fairly good efficiency. For complicated subsurface sensing and imaging cases with smaller FDTD physical domains, nevertheless, one-pole PMLs may not achieve good absorption accuracies so that larger physical domains are required, leading to occupying much more memory and CPU time.

In this paper, to achieve satisfactory absorption accuracies for subsurface sensing and imaging problems and decrease unnecessary FDTD physical regions, an efficient and compact second-order PML with DZT and ME techniques is developed. The proposal is referred to as the DZT-ME-SO-PML. This paper is properly organized as follows: In Section 2, the proposed DZT-ME-SO-PML scheme is developed and introduced. 3D numerical examples, such as the airborne transient electromagnetic (ATEM), are shown in Section 3. In Section 4, for subsurface imaging problems based on measured data detected from the Chang'E-5 Lunar-Exploration Lander, the proposed formulations are used to implement the reverse-time migration (RTM) technique according to the Chang'E-5 Data and help the Chang'E-5 avoid hard rocks when exploring the lunar soil. The conclusions are drawn in Section 4.

2. ME-Based DZT-SO-PML Formulations

For the frequency domain, the modified Maxwell's curl equations can be developed for the three-dimensional second-order PML truncation, shown as

$$\mathrm{j}\omega \boldsymbol{D}(\omega) = \nabla_s \times \boldsymbol{H}(\omega), \tag{1}$$

$$\mathrm{j}\omega \boldsymbol{B}(\omega) \;=\; -\nabla_s \times \boldsymbol{E}(\omega), \tag{2}$$

where

$$\boldsymbol{D} \;=\; \varepsilon_0 \varepsilon_r(\omega)\boldsymbol{E}, \tag{3}$$

$$\boldsymbol{B} \;=\; \mu_0 \mu_r(\omega)\boldsymbol{H}, \tag{4}$$

By applying constitutive relations above, we can obtain and update electric and magnetic fields using $\boldsymbol{D}$ (electric flux density) and $\boldsymbol{B}$ (magnetic flux density) relationship directly due to its full independence of material properties.

As far as we know, the operator ∇_s executed in Equations (1) and (2) can be defined as

$$\nabla_s \;=\; \sum_{\eta\,=\,x,y,z} \boldsymbol{e}_\eta S_\eta^{-1} \partial_\eta, \tag{5}$$

where $S\eta$ ($\eta = x, y, z$) is the n-pole complex stretched coordinate metric, shown below

$$S_\eta \;=\; \prod_{p\,=\,1}^{n} S_{p,\eta} \;=\; \prod_{p\,=\,1}^{n} \left(\kappa_{p,\eta} + \frac{\sigma_{p,\eta}}{\alpha_{p,\eta} + \mathrm{j}\omega\varepsilon_0} \right), \tag{6}$$

It should be noted that we here adopt the SC-PML with the two-pole CFS scheme, and hence the $S\eta$ ($\eta = x, y, z$) is complex stretched coordinate metrics, set as below

$$S_\eta \;=\; \left(\kappa_{1,\eta} + \frac{\sigma_{1,\eta}}{\alpha_{1,\eta} + \mathrm{j}\omega\varepsilon_0} \right) \left(\kappa_{2,\eta} + \frac{\sigma_{2,\eta}}{\alpha_{2,\eta} + \mathrm{j}\omega\varepsilon_0} \right), \tag{7}$$

where $\kappa i,\eta$ must be real and ≥ 1, and $\sigma i,\eta$ and $\alpha i,\eta$ are assumed to be positive real. Now, we re-range and tidy up Equation (7), and have

$$S_\eta \;=\; \prod_{p\,=\,1}^{2} \kappa_{p,\eta} \left(\frac{W_{p,\eta} + \mathrm{j}\omega}{\theta_{p,\eta} + \mathrm{j}\omega} \right) \;=\; \kappa_\eta \left(\frac{W_{1,\eta} + \mathrm{j}\omega}{\theta_{1,\eta} + \mathrm{j}\omega} \right) \left(\frac{W_{2,\eta} + \mathrm{j}\omega}{\theta_{2,\eta} + \mathrm{j}\omega} \right), \tag{8}$$

where

$$\kappa_\eta \;=\; \prod_{p\,=\,1}^{2} \kappa_{p,\eta},\; W_{p,\eta} \;=\; \frac{1}{\varepsilon_0} \left(\alpha_{p,\eta} + \frac{\sigma_{p,\eta}}{\kappa_{p,\eta}} \right), \tag{9}$$

$$\theta_{p,\eta} \;=\; \frac{\alpha_{p,\eta}}{\varepsilon_0}, \tag{10}$$

Then we have

$$S_{p,\eta}^{-1}(\omega) \;=\; \kappa_{p,\eta}^{-1} \left(\frac{W_{p,\eta} + \mathrm{j}\omega + \theta_{p,\eta} - W_{p,\eta}}{W_{p,\eta} + \mathrm{j}\omega} \right) = \xi'^{-1}_{p,\eta} + \frac{\zeta''_{p,\eta}}{v''_{p,\eta} + \mathrm{j}\omega}, \tag{11}$$

where $\xi'^{-1}_{p,\eta} \;=\; \kappa_{p,\eta}^{-1}$, $\zeta''_{p,\eta} \;=\; \kappa_{p,\eta}^{-1}(\theta_{p,\eta} - W_{p,\eta})$, $v''_{p,\eta} \;=\; W_{p,\eta}$, all of them are coefficients in PML regions.

Transform Equation (11) into Z-domain, we obtain

$$S_{p,\eta}^{-1}(\omega) \to S_{p,\eta}(Z) \;=\; \frac{\xi'^{-1}_{p,\eta}}{\Delta t} + \frac{\zeta''_{p,\eta}}{1 - Z^{-1}\exp(-v''_{p,\eta}\Delta t)} = \xi_{p,\eta}^{-1} + \frac{\zeta'_{p,\eta}}{v'_{p,\eta} + Z^{-1}}, \tag{12}$$

where $\xi_{p,\eta}^{-1} \;=\; \frac{\xi'^{-1}_{p,\eta}}{\Delta t}$, $\zeta'_{p,\eta} \;=\; \frac{-\zeta''_{p,\eta}}{\exp(-v''_{p,\eta}\Delta t)}$, $v'_{p,\eta} \;=\; -\exp(v''_{p,\eta}\Delta t)$, all of them are coefficients.

So far, we have finished converting $\mathrm{j}\omega \to s \to Z$. Afterward, we are ready to expand Equations (1) and (2) in the Cartesian coordinates, take y-component for a case

$$Z_T\{\mathrm{j}\omega D_y(\omega)\} \;=\; Z_T\left\{ S_z^{-1}(\omega)\partial_z H_x(\omega) - S_x^{-1}(\omega)\partial_x H_z(\omega) \right\}, \tag{13}$$

Note that $Z_T\{\mathrm{j}\omega\} = \frac{1-Z^{-1}}{\Delta t} = \frac{\partial}{\partial Z}$

$$Z_T\{\mathrm{j}\omega\}Z_T\{D_y(\omega)\} = S_z(Z)Z_T\{\partial_z H_x(\omega)\} - S_x(Z)Z_T\{\partial_x H_z(\omega)\}, \tag{14}$$

$$\frac{\partial D_y(Z)}{\partial Z} = S_z(Z)\partial_z H_x(Z) - S_x(Z)\partial_x H_z(Z), \tag{15}$$

Incorporate $S_\eta(Z)$ into Equation (10) and introduce auxiliary variable ψ and δ, we have

$$\frac{\partial D_y(Z)}{\partial Z} = \left[\xi_z^{-1} + \frac{\zeta'_{1,z}}{v'_{1,z}+Z^{-1}} + \frac{\zeta'_{2,z}}{v'_{2,z}+Z^{-1}}\right]\partial_z H_x(Z) - \left[\xi_x^{-1} + \frac{\zeta'_{1,x}}{v'_{1,x}+Z^{-1}} + \frac{\zeta'_{2,x}}{v'_{2,x}+Z^{-1}}\right]\partial_x H_z(Z), \tag{16}$$

Tide up, and we have

$$\frac{\partial D_y(Z)}{\partial Z} = \xi_z^{-1}\partial_z H_x(Z) - \xi_y^{-1}\partial_y H_z(Z) + \psi_{Dyz} - \psi_{Dyx} + \delta_{Dyz} - \delta_{Dyx}, \tag{17}$$

$$(v'_{1,z}+Z^{-1})\psi_{Dyz}(Z) = \zeta'_{1,z}\partial_z H_x(Z), \tag{18}$$

$$(v'_{1,x}+Z^{-1})\psi_{Dyx}(Z) = \zeta'_{1,x}\partial_x H_z(Z), \tag{19}$$

$$(v'_{2,z}+Z^{-1})\delta_{Dyz}(Z) = \zeta'_{2,z}\partial_z H_x(Z), \tag{20}$$

$$(v'_{2,x}+Z^{-1})\delta_{Dyx}(Z) = \zeta'_{2,y}\partial_y H_x(Z), \tag{21}$$

Now, we further tidy up Equation (17), at first, we add ψ_{Dyz}-ψ_{Dyx} and δ_{Dyz}-δ_{Dyx} in the left-hand side of Equations (18)–(21), and then multiply $1/\Delta t$ for both side, we have

$$\frac{\partial \psi_{Dyz}}{\partial Z} + v_{1,z}\psi_{Dyz} = \zeta_{1,z}\partial_z H_x(Z), \tag{22}$$

$$\frac{\partial \psi_{Dyx}}{\partial Z} + v_{1,z}\psi_{Dyx} = \zeta_{1,x}\partial_x H_z(Z), \tag{23}$$

$$\frac{\partial \delta_{Dyz}}{\partial Z} + v_{2,z}\delta_{Dyz} = \zeta_{2,z}\partial_z H_x(Z), \tag{24}$$

$$\frac{\partial \delta_{Dyx}}{\partial Z} + v_{2,z}\delta_{Dyx} = \zeta_{2,x}\partial_x H_z(Z), \tag{25}$$

where

$$v_{p,\eta} = -\frac{v'_{p,\eta}+1}{\Delta t},\ \zeta_{p,\eta} = -\frac{\zeta'_{p,\eta}}{\Delta t}, \tag{26}$$

Now, all of fields' format can be shown as

$$\omega\frac{\partial \Phi_\eta}{\partial Z} = \xi_{\eta+1}^{-1}\partial_{\eta+1}\Theta_{\eta+2} - \xi_{\eta+2}^{-1}\partial_{\eta+2}\Theta_{\eta+1} + \psi_{\Phi_{\eta(\eta+1)}} - \psi_{\Phi_{\eta(\eta+2)}} + \delta_{\Phi_{\eta(\eta+1)}} - \delta_{\Phi_{\eta(\eta+2)}}, \tag{27}$$

$$\frac{\partial \psi_{\Phi_{\eta(\eta+1)}}}{\partial Z} + v_{1,\eta+1}\psi_{\Phi_{\eta(\eta+1)}} = \zeta_{1,\eta+1}\partial_{\eta+1}\Theta_{\eta+2}(Z), \tag{28}$$

$$\frac{\partial \psi_{\Phi_{\eta(\eta+2)}}}{\partial Z} + v_{1,\eta+2}\psi_{\Phi_{\eta(\eta+2)}} = \zeta_{1,\eta+2}\partial_{\eta+2}\Theta_{\eta+1}(Z), \tag{29}$$

$$\frac{\partial \delta_{\Phi_{\eta(\eta+1)}}}{\partial Z} + v_{2,\eta+1}\delta_{\Phi_{\eta(\eta+1)}} = \zeta_{2,\eta+1}\partial_{\eta+1}\Theta_{\eta+2}(Z), \tag{30}$$

$$\frac{\partial \delta_{\Phi_{\eta(\eta+2)}}}{\partial Z} + v_{2,\eta+2}\delta_{\Phi_{\eta(\eta+2)}} = \zeta_{2,\eta+2}\partial_{\eta+2}\Theta_{\eta+1}(Z), \tag{31}$$

where the symbols ψ and δ are the auxiliary variables, and the symbols Φ and Θ are the substituted electromagnetic fields ($\boldsymbol{E}$ or $\boldsymbol{H}$).

Next, we can get all scalar equations in the following

$$\frac{\partial \boldsymbol{P}}{\partial Z} = \boldsymbol{\Lambda}_1 \cdot \boldsymbol{P} + \boldsymbol{\Lambda}_2 \cdot \boldsymbol{Q}, \tag{32}$$

where

$$\begin{gathered} \boldsymbol{Q} = \begin{bmatrix} \partial_{\eta+1}\boldsymbol{\Theta}_{\eta+2} \\ \partial_{\eta+2}\boldsymbol{\Theta}_{\eta+1} \end{bmatrix}, \boldsymbol{P} = \begin{bmatrix} \varpi\Phi_\eta \\ \psi_{\Phi_{\eta(\eta+1)}} \\ \psi_{\Phi_{\eta(\eta+2)}} \\ \delta_{\Phi_{\eta(\eta+1)}} \\ \delta_{\Phi_{\eta(\eta+2)}} \end{bmatrix}, \\ \boldsymbol{\Lambda}_2 = \begin{bmatrix} \xi_{\eta+1}^{-1} & -\xi_{\eta+2}^{-1} \\ \zeta_{1,\eta+1} & 0 \\ 0 & \zeta_{1,\eta+2} \\ \zeta_{2,\eta+1} & 0 \\ 0 & \zeta_{2,\eta+2} \end{bmatrix}, \boldsymbol{\Lambda}_1 = \begin{bmatrix} 0 & 1 & -1 & 1 & -1 \\ 0 & v_{1,\eta+1} & 0 & 0 & 0 \\ 0 & 0 & v_{1,\eta+2} & 0 & 0 \\ 0 & 0 & 0 & v_{2,\eta+1} & 0 \\ 0 & 0 & 0 & 0 & v_{2,\eta+2} \end{bmatrix} \end{gathered} \tag{33}$$

If the initialize condition t_0 is given, we can obtain below

$$\boldsymbol{P}(t) = \exp[-\boldsymbol{\Lambda}_1(t-t_0)]\{\boldsymbol{P}(t_0) + \int_{t_0}^{t} \exp[\boldsymbol{\Lambda}_1(s-t_0)] \cdot \boldsymbol{\Lambda}_2 \cdot \boldsymbol{Q}\mathrm{d}s\}, \tag{34}$$

By replacing t_0 with the old timestep $n\Delta t$, the above formula in the new timestep $(n+1)\Delta t$ can be expressed as

$$\boldsymbol{P}[(n+1)\Delta t] = \exp[-\boldsymbol{\Lambda}_1 n\Delta t]\{\boldsymbol{P}(n\Delta t) + \int_{n\Delta t}^{(n+1)\Delta t} \exp[\boldsymbol{\Lambda}_1(s-n\Delta t)] \cdot \boldsymbol{\Lambda}_2 \cdot \boldsymbol{Q}\mathrm{d}s\}, \tag{35}$$

Simplify the Equation (25), we can obtain

$$\boldsymbol{P}^{n+1-\frac{1}{2}u(-\varpi)} = \boldsymbol{\Lambda}_3 \boldsymbol{P}^{n-\frac{1}{2}u(-\varpi)} + \boldsymbol{\Lambda}_4 \boldsymbol{Q}^{n+\frac{1}{2}-\frac{1}{2}u(-\varpi)}, \tag{36}$$

where

$$\begin{gathered} \boldsymbol{\Lambda}_3 = \begin{bmatrix} 1 & \gamma'_{2,\eta+1} & -\gamma'_{2,\eta+2} & \gamma''_{2,\eta+1} & -\gamma''_{2,\eta+2} \\ 0 & \gamma'_{1,\eta+1} & 0 & 0 & 0 \\ 0 & 0 & \gamma'_{1,\eta+2} & 0 & 0 \\ 0 & 0 & 0 & \gamma''_{1,\eta+1} & 0 \\ 0 & 0 & 0 & 0 & \gamma''_{1,\eta+2} \end{bmatrix}, \boldsymbol{\Lambda}_4 = \begin{bmatrix} \gamma_{4,\eta+1} & -\gamma_{4,\eta+2} \\ \gamma'_{3,\eta+1} & 0 \\ 0 & \gamma'_{3,\eta+2} \\ \gamma''_{3,\eta+1} & 0 \\ 0 & \gamma''_{3,\eta+2} \end{bmatrix}, \\ \gamma_{1,\eta} = \exp(-v_\eta \Delta t),\ \gamma_{2,\eta} = \frac{\gamma_{1,\eta}-1}{v_\eta},\ \gamma_{3,\eta} = \gamma_{2,\eta}\zeta_\eta, \end{gathered} \tag{37}$$

$$\gamma_{4,\eta} = \frac{\Delta t}{\xi_\eta^{-1}} - \frac{(1-\gamma'_{1,\eta}-v_{1,\eta}\Delta t)\zeta_{1,\eta}}{v_{1,\eta}^2} - \frac{(1-\gamma''_{1,\eta}-v_{2,\eta}\Delta t)\zeta_{2,\eta}}{v_{2,\eta}^2} \tag{38}$$

In FDTD computation, the PML's pseudo code in nth timestep can be expressed in y-direction as follow:

Step 1: The prestore field on the boundary

$$\begin{aligned} C_{1,temp} &= \psi_{Dyz}\big|^{n}_{i,j+\frac{1}{2},k}, \; C_{2,temp} = \psi_{Dyx}\big|^{n}_{i,j+\frac{1}{2},k} \\ C_{3,temp} &= \delta_{Dyz}\big|^{n}_{i,j+\frac{1}{2},k}, \; C_{4,temp} = \delta_{Dyx}\big|^{n}_{i,j+\frac{1}{2},k} \\ C_{5,temp} &= \frac{H_x\big|^{n+\frac{1}{2}}_{i,j+\frac{1}{2},k+\frac{1}{2}} - H_x\big|^{n+\frac{1}{2}}_{i,j+\frac{1}{2},k-\frac{1}{2}}}{\Delta z}, \; C_{6,temp} = \frac{H_z\big|^{n+\frac{1}{2}}_{i+\frac{1}{2},j+\frac{1}{2},k} - H_z\big|^{n+\frac{1}{2}}_{i-\frac{1}{2},j+\frac{1}{2},k}}{\Delta x} \end{aligned} \tag{39}$$

Step 2: Field iteration for D_y

$$\begin{aligned} D_y\big|^{n+1}_{i,j+\frac{1}{2},k} &= D_y\big|^{n}_{i,j+\frac{1}{2},k} + \gamma_{4,z}C_{5,temp} - \gamma_{4,x}C_{6,temp} \\ &+\gamma'_{2,z}\,\psi_{Dyz}\big|^{n}_{i,j+\frac{1}{2},k} - \gamma'_{2,x}\,\psi_{Dyx}\big|^{n}_{i,j+\frac{1}{2},k} \\ &+\gamma''_{2,z}\,\delta_{Dyz}\big|^{n}_{i,j+\frac{1}{2},k} - \gamma''_{2,x}\,\delta_{Dyx}\big|^{n}_{i,j+\frac{1}{2},k} \end{aligned} \tag{40}$$

Step 3: Update the auxiliary quantity

$$\begin{aligned} \psi_{Dyz}\big|^{n+1}_{i,j+\frac{1}{2},k} &= \gamma'_{1,z}C_{1,temp} + \gamma'_{3,z}C_{5,temp} \\ \psi_{Dyx}\big|^{n+1}_{i,j+\frac{1}{2},k} &= \gamma'_{1,x}C_{2,temp} + \gamma'_{3,x}C_{6,temp} \\ \delta_{Dyz}\big|^{n+1}_{i,j+\frac{1}{2},k} &= \gamma''_{1,z}C_{1,temp} + \gamma''_{3,z}C_{5,temp} \\ \delta_{Dyx}\big|^{n+1}_{i,j+\frac{1}{2},k} &= \gamma''_{1,x}C_{2,temp} + \gamma''_{3,x}C_{6,temp} \end{aligned} \tag{41}$$

We have finished mathematical derivations on the DZT-ME-SO-PML, so far.

3. Results and Discussion

3.1. 3D Airborne Transient Electromagnetic Problems

To our knowledge, signals in shorter-wavelength radio waves will be weakened to be neglected when propagating farther and farther, and easily are prohibited by the rock layer. To overcome this problem, the extreme low-frequency electromagnetic wave is considered due to its advantages of long-distance propagation and strong penetration. To validate absorption accuracy of the DZT-ME-SO-PML, 3D numerical simulations on complicated subsurface sensing are carried out.

We consider a 3D dispersive numerical simulation for a half-space problem with three ores distributing at different locations, as shown in Figure 1. The whole computational domain contains air, rock (conductivity σ_{rock} = 0.005 S/m), and mines (conductivity σ_{ore} = 4 S/m), respectively.

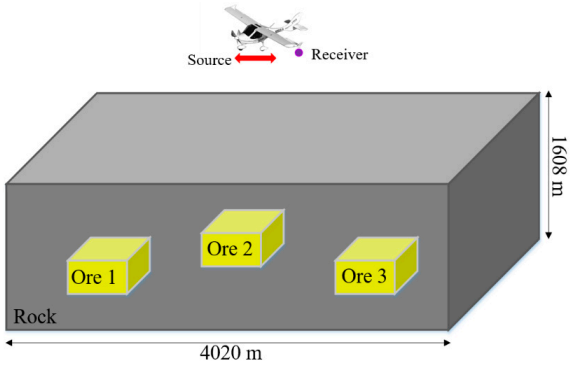

Figure 1. The geometry for a 2-layer medium with three cubic ores in a half space.

Three ore mines (201 m × 201 m × 201 m cubes) are located in the rock region, and their centers of position locate at (2010, 1742, 737) m, (2010, 2010, 804) m, (2010, 2278,

670) m, respectively. The spatial incremental size is discretized with $\Delta x = \Delta y = \Delta z = 67$ m. The whole region is simulated with 4020 m $\times$ 4020 m $\times$ 2010 m. The location of $\boldsymbol{M}_x$ (namely, magnetic point dipole source) is placed in the air at (2010, 2010, 1742) m. The receiving point is placed at (2077, 2077, 1809) m.

Those numerical examples are carried out with the CFS-PMLs ($\alpha_\eta = 0.03$, $\kappa_{\max} = 10$, and $\sigma_{\max} = 4.148$ S/m). For the second-order DZT-PMLs formulations, the following parameters are chosen: $\kappa_{1\eta} = 1$, $\alpha_{1\eta} = 0$, $\sigma_{1\eta,\text{opt}} = 0.175/150\pi\Delta x$, $\sigma_{1\eta,\text{opt}} = \sigma_{1\eta,\text{opt}}\,\rho^4$, $\kappa_{2\eta,\text{opt}} = 12$, $\kappa_{2\eta} = 1 + \kappa_{2\eta,\text{opt}}\,\rho^2$, $\alpha_{2\eta} = 0.02 + \sigma_{1\eta}$, $\sigma_{2\eta,\text{opt}} = 4/150\pi\Delta x$ and $\sigma_{2\eta} = \sigma_{2\eta,\text{opt}}\,\rho^2$, where ρ is zero at the interface of the PML and the FDTD computational domains and 1 at the end.

A bipolar square wave is recognized as the pulse excitation, and then is used with the repetition frequency of 25 Hz (namely, with duration of 0.04 s, rise time 0.0025 s, and fall time 0.0025 s).

It can be observed in Figure 2 that maximum relative reflection errors (MRREs) are respectively -72.81 dB (DZT-PML), -74.99 dB (ME-PML), -101.2 dB (BZT-SO-PML), -101.7 dB (MZT-SO-PML), -111.4 dB (BZT-ME-SO-PML), -112.1 dB (MZT-ME-SO-PML), and -128.1 dB (DZT-ME-SO-PML).

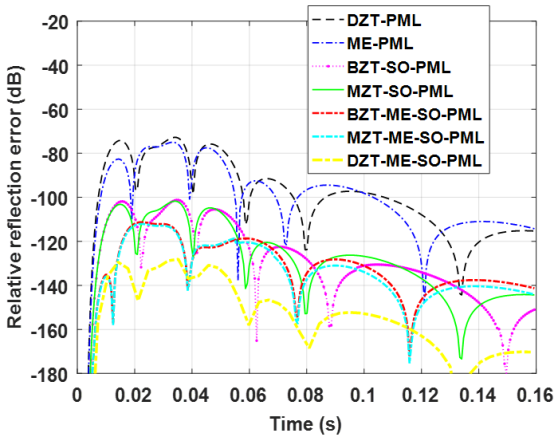

Figure 2. Relative reflection error versus time.

It is concluded in Figure 2 that these PML methods can achieve good effects for an enough FDTD domain. Furthermore, it is clearly seen that the ME-based second-order PMLs can obtain obvious improvements of the MRREs as compared with others. Especially for the DZT-ME-SO-PML method, better absorption performance can be attained due to combining the DZT method than BZT- and MZT-ME-SO-PMLs.

To further indicate the advantage of DZT-ME-SO-PML for absorbing performances, we bring PML boundaries of x and y directions to very close to targets (gap distances between both are changed to 3 cells). As shown in Figure 3, with the obvious reduction of FDTD physical domain, we can witness absorbing performances are influenced evidently, MRREs are respectively -37.55 dB (DZT-PML), -41.99 dB (ME-PML), -50.30 dB (BZT-SO-PML), -51.0 dB (MZT-SO-PML), -57.35 dB (BZT-ME-SO-PML), -58.15 dB (MZT-ME-SO-PML), and -67.68 dB (DZT-ME-SO-PML). As shown in Figure 3, the relative errors of all PMLs become larger apparently, when physical domains get smaller.

It can be concluded from the numerical result in Figure 3 that the DZT-PML cannot meet the engineering requirement (below -40 dB) due to using smaller domain; the ME-PML becomes much weaker than SO-PMLs based on Z-transform methods, in aspect of absorbing performance, due to existing strong propagating and evanescent waves; the absorption accuracies of Z-transform based SO-PMLs are improved at the price of more complex iteration forms and lower computational efficiency, in spite of obvious reductions for both early- and late-time reflections; To improve this problem, the ME technique is introduced into the BZT- and MZT-SO-PMLs so that higher efficiency is obtained; However, to our knowledge, the DZT approach can achieve the most accuracy as compared with the BZT and MZT, therefore, to sum up, the proposed ME-based DZT-SO-PML is developed to

overcome these problems, resulting in achieving satisfactory accuracies and efficiencies for any general problems.

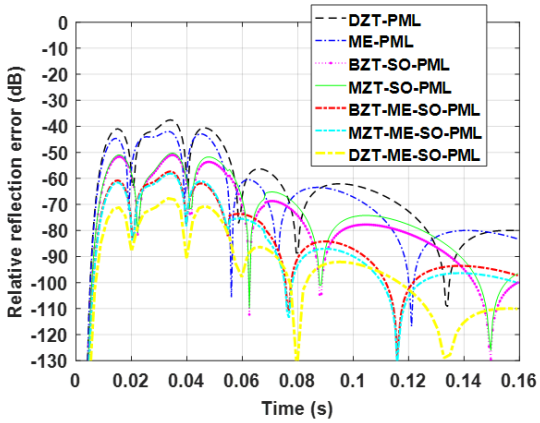

Figure 3. Relative reflection error versus time for a smaller physical domain.

Next, to illustrate robustness and validity of the proposed method, the 3D subsurface imaging problem for measured data from Chang'E-5 lunar-exploration Lander is considered. To the best of our knowledge, the Chang'E-5 Project are going to be launched to explore a lunar subsurface region and take lunar geological samples back to the earth in the near future. Consequently, it is necessary to implement the high-resolution subsurface imaging firstly in the earth laboratory.

3.2. DZT-ME-SO-PML-Based FDTD Applied to the Reverse-Time Migration Method

The RTM method is the most reliable exploration methods in geological structure prediction. In 2020, the Chang'E-5 is planned for the first time to drill lunar soil in the moon, and then return it to earth, which is the most critical exploration mission in China's lunar exploration project. Due to the inevitable collision of those hard rocks during lunar-soil drilling, the purpose of the RTM method is to predict the distribution information of hard rocks in the soil in advance, so as to prevent the drill bit damage from affecting the soil-drilling task of the Chang'E-5. The RTM method must be based on multiple calculations with FDTD as the underlying forward code, so we apply the DZT-ME-SO-PML scheme as its absorbing boundary condition to obtain the subsurface imaging.

In Chang'E-5, to transmit the broadband pulses and to obtain subsurface information, we employed 12 Vavaldi antennas as the basic element on its ground penetrating radar. As shown in Figure 4, the transmitted signals of 12 antennas from Table 1 can be measured and the time-domain pulse signal waveform is easily obtained.

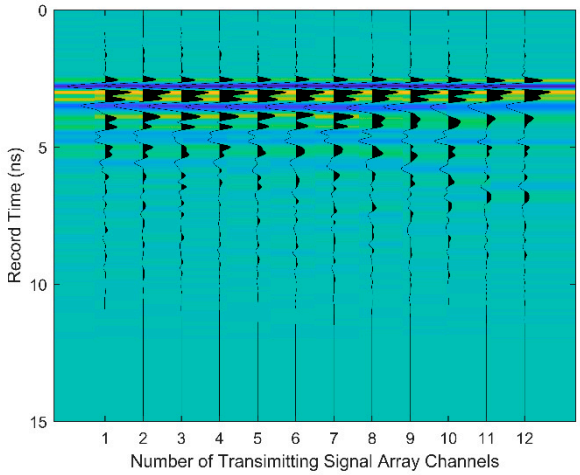

Figure 4. Waveforms of transmitting signals from 12 Vavaldi antennas on Chang'E-5.

Table 1. The specific positions of Chang'E-5 Antennas.

No.	Position (m)	No.	Position (m)	No.	Position (m)	No.	Position (m)
1	(−0.80, 0.00, 0.95)	4	(−0.44, 0.00, 0.95)	7	(−0.08, 0.00, 0.95)	10	(0.76, 0.00, 0.95)
2	(−0.68, 0.00, 0.95)	5	(−0.32, 0.00, 0.95)	8	(0.52, 0.00, 0.95)	11	(0.52, 0.12, 0.95)
3	(−0.56, 0.00, 0.95)	6	(−0.20, 0.00, 0.95)	9	(0.64, 0.00, 0.95)	12	(−0.02, 0.18, 1.13)

In the past study [31–35], the property of the lunar soil was initially defined as the permittivity $\varepsilon_r = 3$. To model the lunar environment, we adopt the $\varepsilon_r = 3$ volcanic ash instead of the lunar soil as the background media. As shown in Figure 5a,b, two single-station laboratory data from an experimental lunar exploration system Chang'E-5 are extracted, and the subsurface laboratory model is filled with the volcanic ash in 2.5 m × 2.0 m × 1.0 m experiment region. In the process of measurement in the earth laboratory, a PEC barrier is placed at 2.5 m to block the unknown electromagnetic echoes that may be transmitted upward. According to the signal transmitted by one antenna and received by 11 antennas at the same time, the received data of 12 × 11 = 132 channels were effectively obtained by transmitting in turn. Those measurement results are shown in Figure 6.

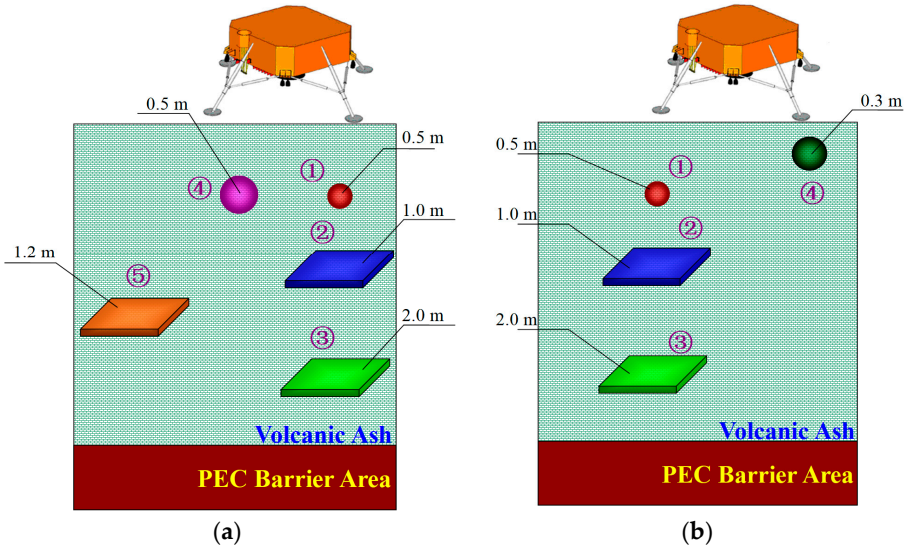

(**a**) (**b**)

Figure 5. Two single-station laboratory data acquisition systems from an experimental lunar exploration system Chang'E-5. The $\varepsilon_r = 3$ volcanic ash replaces lunar soil as background for buried objects. In (**a**), the buried objects are respectively ① Basalt, ② Teflon, ③⑤ Granite and ④ Metal. In (**b**), the buried objects are respectively ① Basalt, ② Teflon, and ③④ Granite.

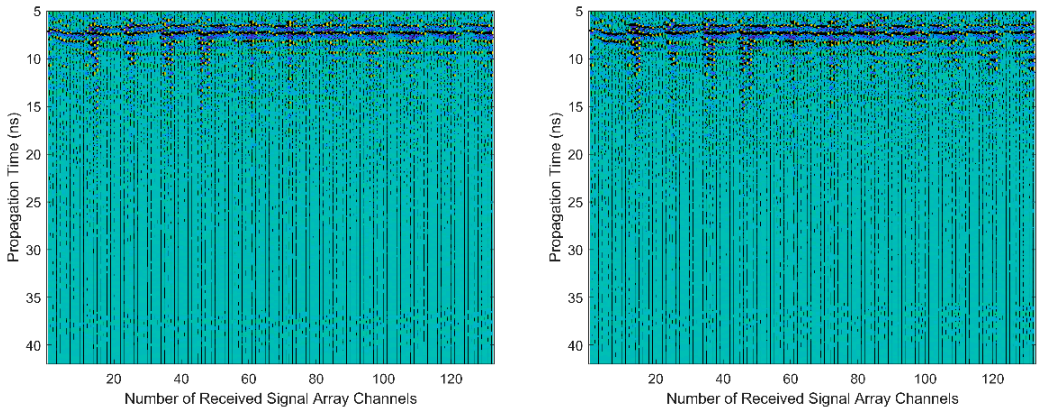

(**a**) (**b**)

Figure 6. Two single-station laboratory original measured data based on the experiment model: (**a**) for Figure 5a, and (**b**) for Figure 5b, respectively.

It can be seen from Figure 6 that the amplitude of the underground electromagnetic echo decreases with the increase of the receiving time of the antenna echo signal, and the underground electromagnetic signal cannot be understood even after the data is amplified. Hence the transmitting antenna can be considered as an electric dipole in a long distance area, so that the received data can be post processed. For a more intuitive understanding of subsurface information, the relation between echo dataset and propagation time is adjusted below

$$D_{opti} = D_{meas} \times t_{prop}^2 \tag{42}$$

where D_{meas} and D_{opti} are respectively the initial measured data and the optimal measured data. We can obtain the distribution of received data as shown in Figure 7. Obviously, the PEC barrier area buried at 2.5 m underground produces strong electromagnetic reflection and is received by antenna equipment, but the distribution of buried targets is still uncertain.

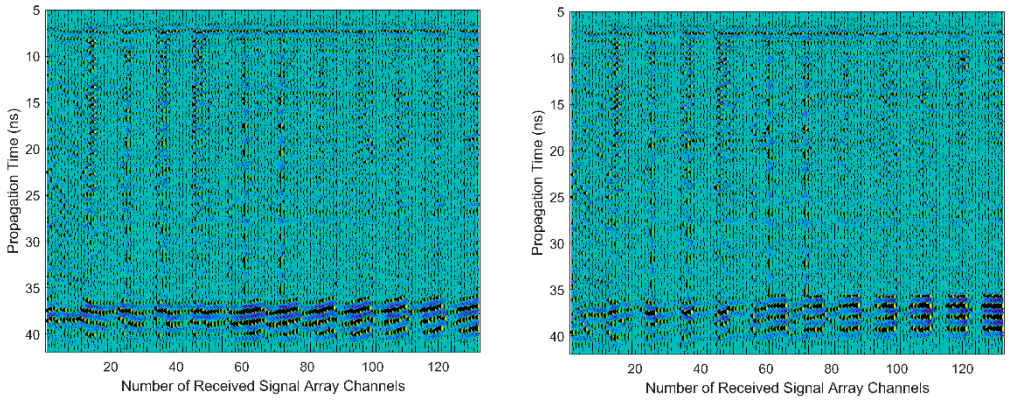

(**a**) (**b**)

Figure 7. Two single-station measured data after the optimal Equation (36): (**a**) for Figure 5a, and (**b**) for Figure 5b, respectively.

In the real laboratory measurement, excitation signals can be transmitted from the Chang'E-5's UWBR system and recorded from the channel antenna. After the Chang'E-5 measurement is finished, the DZT-ME-SO-PML method can be applied to implement the subsurface imaging, shown in Figure 8a,b. The aim of reverse-time migration is to find the buried objection in approximate location and help the Chang'E-5 to avoid the hard rocks. The specific shape cannot be restored unless the signal is without any noises. The two different responses for the PEC are occurred because the different electromagnetic echoes come from different paths through the different buried objects and different antenna locations. Consequently, it further corroborates the validity and accuracy of the proposal.

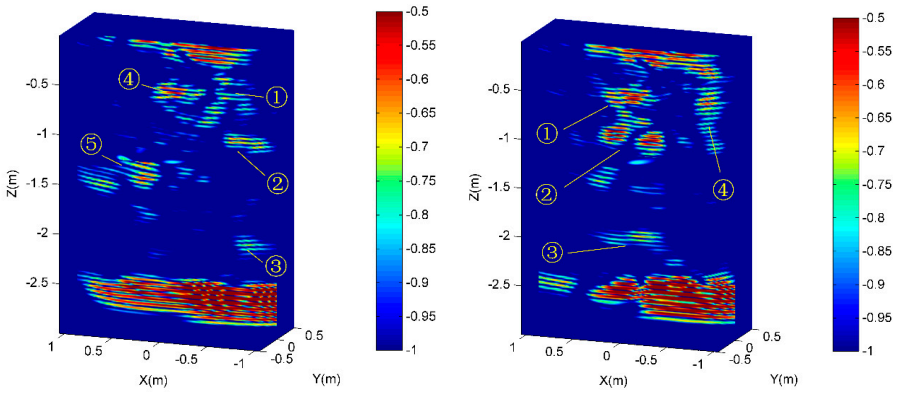

(**a**) (**b**)

Figure 8. RTM results for the Chang'E-5 UWBR system experimental data based on the DZT-ME-SO-PML method, (**a**) for Figure 5a, and (**b**) for Figure 5b, respectively.

4. Conclusions

This study reveals a reliable fact that we can make full use of the DZT-ME-SO-PML-based FDTD method for implementing the subsurface sensing and imaging problems. We introduce the ME technique for developing a compact first-order differential matrix form, incorporate the DZT method into the PML-based FDTD for achieving higher accuracy, and consider the second-order PML ABC for obtaining better absorption performance, for solving the 3D subsurface sensing and imaging problems.

The findings of this study can be summarized as follows:

1. The proposed DZT-ME-SO-PML scheme could not only attenuate the strong propagating wave, but also absorb the evanescent wave and reduce late-time reflection, for 3D subsurface sensing.
2. The DZT-ME-SO-PML-based FDTD can be applied to the RTM method so that the distribution information of hard rocks in the soil can be predicted in advance, in order to prevent the drill bit damage from affecting the soil-drilling task of the Chang'E-5.
3. For the ATEM problems, we could achieve the secondary-field data from the receiver, analyze the distribution of scattering field, and finally predict the location of objects.

Author Contributions: Conceptualization, N.F. and Y.Z.; methodology, N.F. and Y.Z.; formal analysis, N.F. and Q.Z.; writing—original draft preparation, N.F.; writing—review and editing, N.F., Y.Z., G.P.W., Q.Z., W.T.J. All authors have read and agreed to the published version of the manuscript.

Funding: This research is funded by the National Natural Science Foundation of China under Grant 61901274, and 11734012, the Natural Science Foundation of Guangdong Province under Grant 2020A1515010467, the Shenzhen Science and Technology Innovation Committee under Grant No. JCYJ20190808141818890, and the Open Fund of State Key Laboratory of Applied Optics under Grant SKLAO2020001A06.

Institutional Review Board Statement: Not applicable.

Informed Consent Statement: Not applicable.

Data Availability Statement: No new data were created or analyzed in this study. Data sharing is not applicable to this article.

Acknowledgments: The authors gratefully acknowledge Guangyou Fang now working in Aerospace Information Research Institute, Chinese Academy of Sciences for the assistance in providing the CE-5 data and helpful discussions.

Conflicts of Interest: The authors declare no conflict of interest.

References

1. Ayhan, S.; Pauli, M.; Scherr, S.; Göttel, B.; Bhutani, A.; Thomas, S.; Jaeschke, T.; Panel, J.M.; Vivier, F.; Eymard, L.; et al. Millimeter-Wave Radar Sensor for Snow Height Measurements. *IEEE Trans. Geosci. Remote Sens.* **2017**, *55*, 854–861. [CrossRef]
2. Wehling, J.H. Multifunction millimeter-wave systems for armored vehicle application. *IEEE Trans. Microw. Theory Tech.* **2005**, *53*, 1021–1025. [CrossRef]
3. Freundorfer, A.P.; Iizuka, K. A study on the scattering of radio waves from buried spherical targets using the step frequency radar. *IEEE Trans. Geosci. Remote Sens.* **1993**, *31*, 1253–1255. [CrossRef]
4. Moallem, M.; Sarabandi, K. Polarimetric Study of MMW Imaging Radars for Indoor Navigation and Mapping. *IEEE Trans. Antennas Propagat.* **2014**, *62*, 500–504. [CrossRef]
5. Nelson, L.M.; Levine, J. Understanding limitations of GPS carrier phase frequency transfer on a transatlantic baseline. In Proceedings of the 2001 IEEE International Frequency Control Symposium and PDA Exhibition, Seattle, WA, USA, 8 June 2001; pp. 205–210.
6. Kemp, M.A.; Franzi, M.; Haase, A.; Jongewaard, E.; Whittaker, M.T.; Kirkpatrick, M.; Sparr, R. A high Q piezoelectric resonator as a portable VLF transmitter. *Nat. Commun.* **2019**, *10*, 1715. [CrossRef] [PubMed]
7. Cui, T.J.; Chew, W.C. Accurate analysis of wire structures from very-low frequency to microwave frequency. *IEEE Trans. Antennas Propagat.* **2002**, *50*, 301–307.
8. Yee, K. Numerical solution of initial boundary value problems involving maxwell equations in isotropic media. *IEEE Trans. Antennas Propagat.* **1966**, *AP-14*, 302–307.
9. Elsherbeni, A.Z.; Demir, V. *The Finite-Difference Time-Domain Method for Electromagnetics with Matlab Simulations*, 2nd ed.; SciTECH Publishing: Norwood, NJ, USA, 2015; pp. 1–27.

10. Bérenger, J.P. A perfectly matched layer for the absorption of electromagnetic waves. *J. Computat. Phys.* **1994**, *114*, 185–200. [CrossRef]
11. Roden, J.A.; Gedney, S.D. Convolution PML (CPML): An efficient FDTD implementation of the CFS-PML for arbitrary media. *Microw. Opt. Technol. Lett.* **2000**, *27*, 334–339. [CrossRef]
12. Ramadan, O. Auxiliary differential equation formulation: An efficient implementation of the perfectly matched layer. *IEEE Microw. Wirel. Compon. Lett.* **2003**, *13*, 69–71. [CrossRef]
13. Li, J.; Dai, J. An efficient implementation of the stretched coordinate perfectly matched layer. *IEEE Microw. Wirel. Compon. Lett.* **2007**, *17*, 322–324. [CrossRef]
14. Sullivan, D.M. Frequency-dependent FDTD methods using Z transforms. *IEEE Trans. Antennas Propag.* **1992**, *40*, 1223–1230. [CrossRef]
15. Ramadan, O.; Oztoprak, A.Y. Z-transform implementation of the perfectly matched layer for truncating FDTD domains. *IEEE Microw. Wirel. Compon. Lett.* **2003**, *13*, 402–404. [CrossRef]
16. Kuzuoglu, M.; Mittra, R. Frequency dependence of the constitutive parameters of causal perfectly matched anisotropic absorbers. *IEEE Microw. Guided Wave Lett.* **1996**, *6*, 447–449. [CrossRef]
17. Berenger, J.P. Evanescent waves in PML's: Origin of the numerical reflection in wave-structure interaction problems. *IEEE Trans. Antennas Propag.* **1999**, *47*, 1497–1503. [CrossRef]
18. Berenger, J.P. Numerical reflection from FDTD-PMLs: A comparison of the split PML with the unsplit and CFS PMLs. *IEEE Trans. Antennas Propag.* **2002**, *50*, 258–265. [CrossRef]
19. Feng, N.; Yue, Y.; Zhu, C.; Liu, Q.H.; Wan, L. Efficient Z-Transform Implementation of the D-B CFS-PML for Truncating Multi-term Dispersive FDTD Domains. *Appl. Comput. Electrom.* **2014**, *29*, 190–196.
20. Gedney, S.D.; Zhao, B. An Auxiliary Differential Equation Formulation for the Complex-Frequency Shifted PML. *IEEE Trans. Antennas Propagat.* **2010**, *58*, 838–847. [CrossRef]
21. Giannopoulos, A. An improved new implementation of complex frequency shifted PML for the FDTD method. *IEEE Trans. Antennas Propag.* **2008**, *56*, 2995–3000. [CrossRef]
22. Correia, D.; Jin, J.M. Performance of regular PML, CFS-PML, and second-order PML for waveguide problems. *Microw. Opt. Technol. Lett.* **2006**, *48*, 2121–2126. [CrossRef]
23. Correia, D.; Jin, J.M. On the development of a higher-order PML. *IEEE Trans. Antennas Propag.* **2005**, *53*, 4157–4163. [CrossRef]
24. Giannopoulos, A. Unsplit implementation of higher order PMLs. *IEEE Trans. Antennas Propag.* **2012**, *60*, 1479–1485. [CrossRef]
25. Feng, N.; Li, J.; Zhao, X. Efficient FDTD implementation of the higher-order PML using DSP techniques for arbitrary media. *IEEE Trans. Antennas Propag.* **2013**, *61*, 2623–2629. [CrossRef]
26. Feng, N.; Li, J. Efficient DSP-higher-order PML formulations for the metal plate buried in dispersive soil half-space. *IEEE Trans. Electromagn. Compact.* **2012**, *54*, 1178–1181. [CrossRef]
27. Feng, N.; Li, J. Novel and efficient FDTD implementation of higher-order perfectly matched layer based on ADE method. *J. Computat. Phys.* **2013**, *232*, 318–326. [CrossRef]
28. Feng, N.; Yue, Y.; Zhu, C.; Wan, L.; Liu, Q.H. Second-order PML: Optimal choice of nth-order PML for truncating FDTD domains. *J. Computat. Phys.* **2015**, *285*, 71–83. [CrossRef]
29. Feng, N.; Yue, Y.; Liu, Q.H. Direct Z-transform Implementation of the CFS-PML based on Memory- minimized method 2015. *IEEE Trans. Microw. Theory Tech.* **2015**, *63*, 877–882. [CrossRef]
30. Jiang, H.; Zhang, J.; Cui, T.J. An Alternative PML Implementation for Arbitrary Media. *IEEE Trans. Antennas Propag.* **2019**, *67*, 612–615. [CrossRef]
31. Zhang, Y.; Wang, L.; Feng, N.; Zhuang, M.; Feng, X.; Fang, G.; Liu, Q.H. A 3-D High-Order Reverse-Time Migration Method for High-Resolution Subsurface Imaging with a Multistation Ultra-Wideband Radar System. *IEEE J.-STARS* **2019**, *12*, 744–751. [CrossRef]
32. Fa, W.; Zhu, M.H.; Liu, T.; Plescia, J.B. Regolith stratigraphy at the Chang'e-3 landing site as seen by lunar penetrating radar. *Geophys. Res. Lett.* **2015**, *42*, 10179–10187. [CrossRef]
33. Wang, Z.; Wu, Y.; Blewett, D.T.; Cloutis, E.A.; Zheng, Y.; Chen, J. Submicroscopic metallic iron in lunar soils estimated from the in situ spectra of the Chang'e-3 mission. *Geophys. Res. Lett.* **2017**, *44*, 3485–3492. [CrossRef]
34. Liu, D.; Zhang, Y.; Zhang, G.; Liu, B.; Ren, X.; Xu, R.; Li, C. An Empirical Model to Estimate Abundance of Nanophase Metallic Iron (npFe0) in Lunar Soils. *Remote Sens.* **2020**, *12*, 1047. [CrossRef]
35. Qi, X.; Ling, Z.; Zhang, J.; Chen, J.; Cao, H.; Liu, C.; Qiao, L.; Fu, X.; He, Z.; Xu, R.; et al. Photometric Normalization of Chang'e-4 Visible and Near-Infrared Imaging Spectrometer Datasets: A Combined Study of In-Situ and Laboratory Spectral Measurements. *Remote Sens.* **2020**, *12*, 3211. [CrossRef]